

# Characterization of 3-phase (ternary-like) n-type and p-type thermoelectric materials fabricated by explosive (shock-wave) consolidation

V.B. Muñoz<sup>a,b</sup>, L.E. Murr<sup>a,\*</sup>, D. Nemir<sup>c</sup>, R. Lourenich<sup>c</sup>, E. Rubio<sup>c</sup>,  
E.Y. Martinez<sup>a</sup>, S.M. Gaytan<sup>a</sup>, M.I. Lopez<sup>a</sup>

<sup>a</sup>Department of Metallurgical and Materials Engineering, The University of Texas at El Paso, El Paso, TX 79968, USA

<sup>b</sup>OSRAM Sylvania Inc., Juarez 32470, Mexico

<sup>c</sup>TXL Group, Inc., El Paso, TX 79903, USA

## ARTICLE DATA

### Article history:

Received 15 October 2007

Accepted 22 October 2007

### Keywords:

Shock consolidation

Thermoelectric materials

Microstructures

Materials characterization

## ABSTRACT

Three-phase powder mixtures of Bi–Te–Se and Bi–Te–Sb were prepared by cylindrical explosive consolidation to emulate traditional, melt-grown n-type and p-type doped  $\text{Bi}_2\text{Te}_3$  thermoelectric materials. The powder diameters ranged from 40  $\mu\text{m}$  to 3  $\mu\text{m}$ , with starting Bi and Te particle Vickers microindentation hardnesses of 0.18 and 0.56 GPa, respectively, in contrast to average shocked n-type and p-type monolith microindentation hardnesses of 1.15 and 1.31 GPa, respectively. The values may also be contrasted to 0.72 and 0.68 GPa hardnesses for melt-grown n-type and p-type materials, respectively. Shock consolidated monolith microstructures were characterized by optical metallography, SEM and TEM along with EDS analysis and XRD of all materials, including the melt-grown materials which had measured thermoelectric parameters considerably in excess of the shock (explosively) consolidated monoliths. Notable shock microstructures were characterized by deformation twins, while the melt-grown materials contained considerable, fine eutectic microstructures. These shock-grown microstructures do not appear to be conducive to thermoelectric figure of merit optimization.

© 2007 Elsevier Inc. All rights reserved.

## 1. Introduction

Since electrons in solids are energy carriers as well as electric charge carriers, thermal effects can produce electrical effects and vice versa. Thermoelectric (TE) generation is the conversion of heat energy to electrical energy. When a temperature difference exists along a conductor, it causes mobile charge carriers (electrons and/or holes) to migrate from hot to cold. The resulting separation of charge creates an electric field potential known as the Seebeck voltage, that is given by  $\Delta V = S \Delta T$ , where  $S$  is a temperature-dependent material property known as the Seebeck coefficient and, by convention,  $\Delta T$  represents the temperature of the cold side with respect to the

hot side. The Seebeck coefficient for a material may be positive or negative, depending upon doping. When an external voltage is applied to a TE element, it will create a thermal gradient, yielding Peltier heating or cooling, depending upon the voltage polarity.

For thermoelectric generation, it is common to use doped alloys of tellurium as the active elements for converting thermal energy to electrical energy. Doped bismuth telluride alloys are the most popular for the temperature range of about 220 K to 420 K and have the attractive properties of a relatively high Seebeck coefficient,  $S$ , a relatively high electrical conductivity,  $\sigma$ , and a relatively low thermal conductivity,  $K = K_{\text{el}} + K_{\text{ph}}$ , where  $K_{\text{el}}$  is the electronic thermal conductivity and  $K_{\text{ph}}$  is

\* Corresponding author. Tel.: +1 915 747 6929; fax: +1 915 747 8036.  
E-mail address: [fekberg@utep.edu](mailto:fekberg@utep.edu) (L.E. Murr).

**Table 1 – Thermoelectric semiconductor precursor properties and composition**

Element	Nominal particle size ( $\mu\text{m}$ )	Hardness (GPa)	Purity (%)	n-type composition (wt.%)	p-type composition (wt.%)
Bi	40	0.18	99.99	53	16
Te	30	0.56	99.70	44	57
Sb	6	–	99.99	–	27
Se	3	–	99.90	3	–

Note that 1 GPa = 100 VHN (Vickers Hardness Number).

the phonon (or lattice) thermal conductivity. These bulk material properties are often lumped into a single dimensionless figure of merit  $ZT$ , where  $T$  is temperature in degrees Kelvin and

$$ZT = \frac{T(S^2\sigma)}{(K_{\text{el}} + K_{\text{ph}})}.$$

The term  $S^2\sigma$  is often referred to as the power factor, which characterizes the energy conversion ability of the material.  $S$ ,  $\sigma$ , and  $K_{\text{el}}$  are essentially interrelated and all are determined by the electron transport properties, since  $K_{\text{el}}$  and  $\sigma$  are proportional to the mean free path (or scattering) of the electrons.

The better figures of merit range around unity for  $\text{Bi}_2\text{Te}_3$  and variously doped  $\text{Bi}_2\text{Te}_3$ , nominal ternary compositions such as  $\text{Bi}_{2.7}\text{Se}_{0.3}$  and  $\text{Bi}_{0.5}\text{Sb}_{1.5}\text{Te}_3$ : n-type and p-type, respectively; where  $S=220 \mu\text{V/K}$  [1, 2]. But, for the conversion of waste heat to electricity to be efficient (>20%), or for a thermoelectric device to compete with traditional cooling technologies,  $ZT \geq 3$  is required.. To raise the figure of merit requires  $\sigma$  (or  $S^2\sigma$ ) to be large so energy is not wasted, and at the same

time the thermal conductivity ( $K_{\text{el}} + K_{\text{ph}}$ ) must be small so that heat transported to the hot end (or temperature reference) of the device remains there. This manipulation of thermal transport in materials may allow for the development of high efficiency thermoelectric (solid-state) refrigerators and power generators [3].

Extremes of electrical conductivity ( $\sigma$ ) in materials now span roughly 25 orders of magnitude (from  $6.8 \times 10^7 (\Omega \text{ m})^{-1}$  for Ag to  $1.3 \times 10^{-18} (\Omega \text{ m})^{-1}$  for  $\text{SiO}_2$ -glass) in contrast to the thermal conductivity of solid-state materials at room temperature which spans only 4 orders of magnitude; the lowest thermal conductivities occur in alloys, especially semiconductor alloys, because the atomic substitutions significantly scatter phonons, leading to a short mean free path. These values range from 5 W/mK to 10 W/mK (at room temperature). Of course dislocations and other defects in crystalline materials which scatter electrons also scatter phonons, and scattering is therefore the key, or at least a key, to thermoelectric optimization; since on the one hand we require low scattering and large mean free path for electrons, and correspondingly large

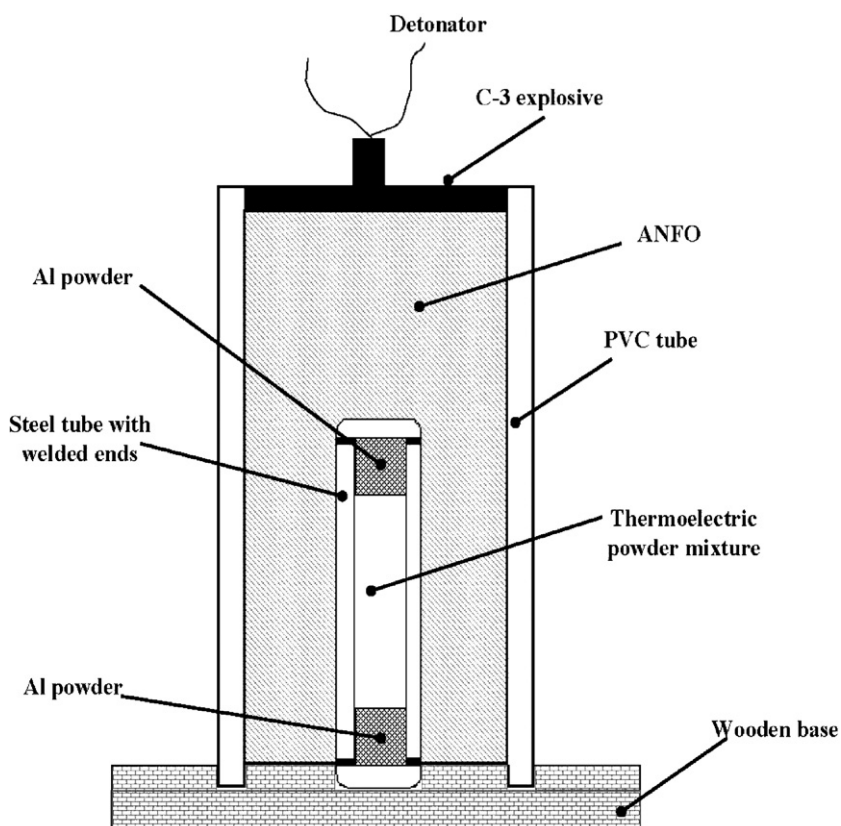


Fig. 1 – Schematic diagram illustrating cylindrical explosive powder consolidation arrangement.

scattering and small mean free path for phonons. Using nanostructures and nanocompositions has also demonstrated a workable strategy [4–6]. Since substitutional atoms, or impurities in particular, scatter short-wavelength phonons more effectively than long-wavelength phonons, the latter dominate heat conduction in semiconductor alloys. Correspondingly, amorphous materials limit the mean free path to only a few lattice spacings, causing extremely low thermal conductivity (1.3 W/mK to 3 W/mK) at room temperature [7]. The mean free path associated with lattice thermal conductivity ( $K_{ph}$ ) is a function of both intrinsic (phonon-phonon) and extrinsic (phonon-defect) scattering.

The effects of crystal defects on optimizing electrical and thermal conductivity is complex and there is little, if any, microstructural characterization of thermoelectric materials, although Zou et al. [8] have studied the dependency of  $K_{ph}$  on dislocation and point defect densities in GaN where a narrow range of dislocation densities influenced  $K_{ph}$ . Crystal (grain) boundary scattering has also been studied [2, 9, 10]. Slack and Hussein [10] observed a small increase in ZT for grain sizes < 2 μm in Si-Ge alloys, but further reductions in grain size drastically reduced ZT. Some of the main gains in increasing ZT have been based on strategies to reduce thermal conductivity by increasing the density of interfaces, including grain boundaries, which scatter phonons more effectively than electrons [11].

In this study, we utilized explosive-shock consolidation of 3-phase powder mixtures coupled with detailed microstructural characterization to explore novel thermoelectric materials development. Mixtures of Bi, Te and Se powders were used to emulate the n-type ternary (alloy) system  $Bi_2Te_{2.7}Se_{0.3}$ , and mixtures of Bi, Sb and Te powders were used to emulate the p-type ternary (alloy) system  $Bi_{0.5}Sb_{1.5}Te_3$ . These n-type and p-type shock-consolidated monoliths were compared with standard, melt grown n-type and p-type ternary materials, all characterized using optical metallography, SEM, XRD, TEM and Vickers microindentation hardness. The figures of merit (ZT) and corresponding Seebeck voltages were also measured and compared.

## 2. Experimental Details

In a polycrystalline semiconductor alloy the microstructures, particularly defects (including interfaces), contribute to electron and phonon scattering. In this study we considered a novel approach to creating a thermoelectric (ternary-like) material. Rather than a conventional melt-grown semiconductor alloy (n or p-type) we explored the concept of “an interfacial composite” or multi-phase system emulating a conventional alloy composition with the prospect to provide new insights into thermoelectric device fabrication and performance.

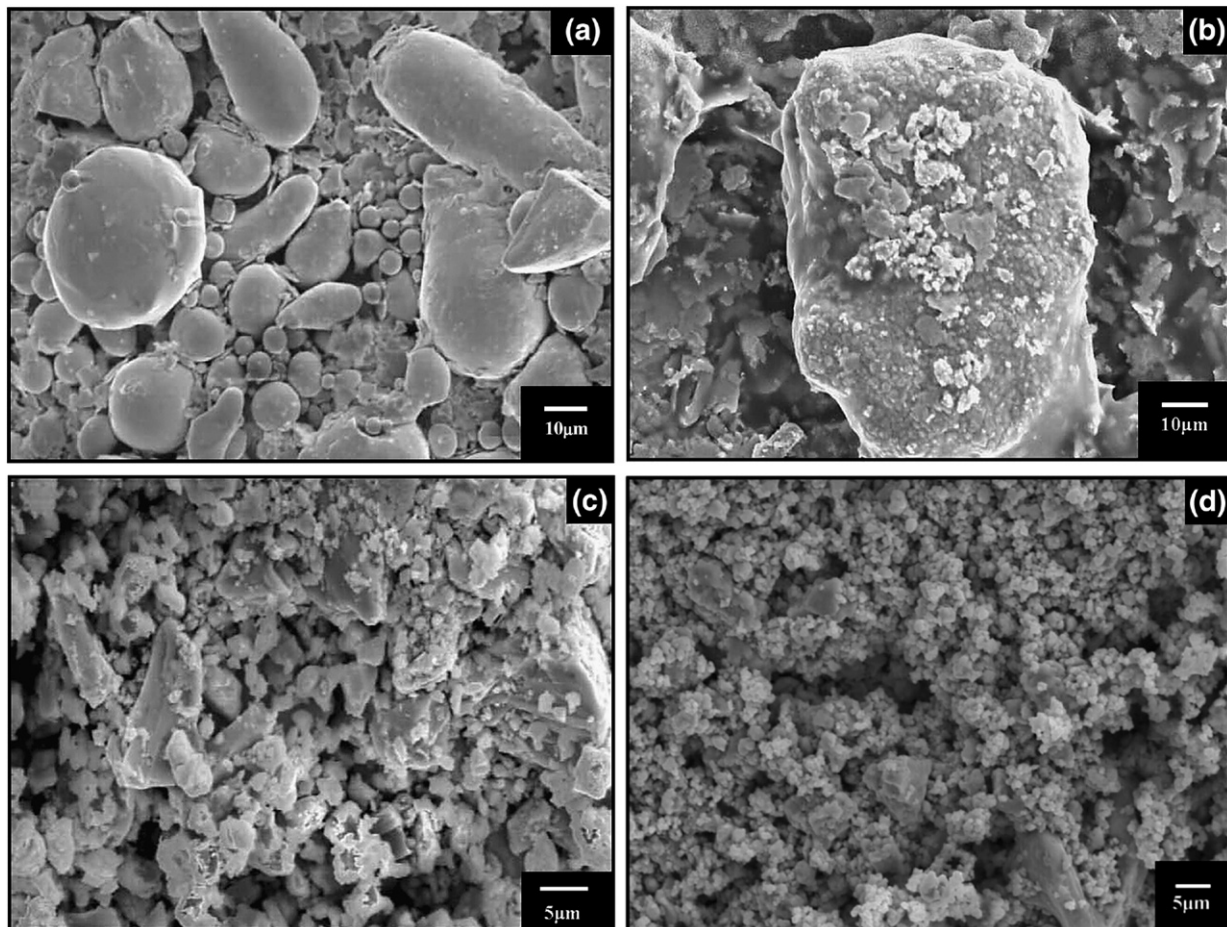


**Fig. 2 – SEM views of starting (a) bismuth, (b) tellurium, (c) antimony and (d) selenium powders.**

Conventional alloy systems are based on the performance of  $\text{Bi}_2\text{Te}_3$  materials which are tailored by the introduction of dopant elements in solution. Selenium is generally added to form an n-type material yielding a negative Seebeck coefficient ( $-S$ ), while the addition of Sb results in a p-type material with a positive Seebeck coefficient ( $+S$ ). In contrast to metals which may have a Seebeck coefficient of up to a few tens of microvolts/K, doped  $\text{Bi}_2\text{Te}_3$  elements have Seebeck coefficients in the hundreds of microvolts/K. This still leads to a fairly small generated voltage per thermoelectric element, requiring that practical thermoelectric devices be composed of multiple thermoelectric elements configured to be electrically in series and thermally in parallel. Consequently, we produced powder mixtures of Bi, Te, and Se to emulate n-type, ternary  $\text{Bi}_2\text{Te}_{2.7}\text{Se}_{0.3}$ , and Bi, Sb and Te to emulate p-type, ternary  $\text{Bi}_{0.5}\text{Sb}_{1.5}\text{Te}_3$  thermoelectric semiconductor materials, using nominal mean powder particle sizes and purities illustrated in Table 1. Table 1 also shows the nominal compositions for the n-type and p-type mixtures in weight percent. Well-mixed powders (n-type and p-type compositions shown in Table 1) were compacted into 2.5 cm (inner) diameter steel tubes 28 cm in length, with 2.5 cm compacted aluminum powder (nomin-

ally 150  $\mu\text{m}$  particle diameter) at each end, and steel caps welded to the ends. These tubes were placed in PVC cylinders nominally 35 cm in diameter and 38.5 cm in height, and filled with an ammonium nitrate-fuel oil (ANFO) mix as illustrated schematically in Fig. 1. A circular sheet of composition C-3 high explosive was placed at the top of the ANFO and an electric detonator placed in the center of the C-3 sheet (Fig. 1). When detonated over sand bags, the consolidated powder compositions within the steel tubes were recovered on the ground at the point of detonation. Cylindrical shock-wave consolidation arrangements characteristic of that shown in Fig. 1 have been described in detail by Prümmer [12] and Meyers and Wang [13] among others [14]. These experiments were performed at the Energetic Materials Research and Testing Center at New Mexico Tech, Socorro, New Mexico. The shock pressure associated with these explosive consolidation experiments was  $\sim 4$  GPa, based on an ANFO detonation velocity of 2 km/s [12, 14]. The steel tubes were machined from the n- or p-type consolidated cylinders, and sections cut from the cylinders for test and analysis.

X-ray diffraction (XRD) was done on elemental powders, n- and p-type powder combinations (mixtures in Table 1), the

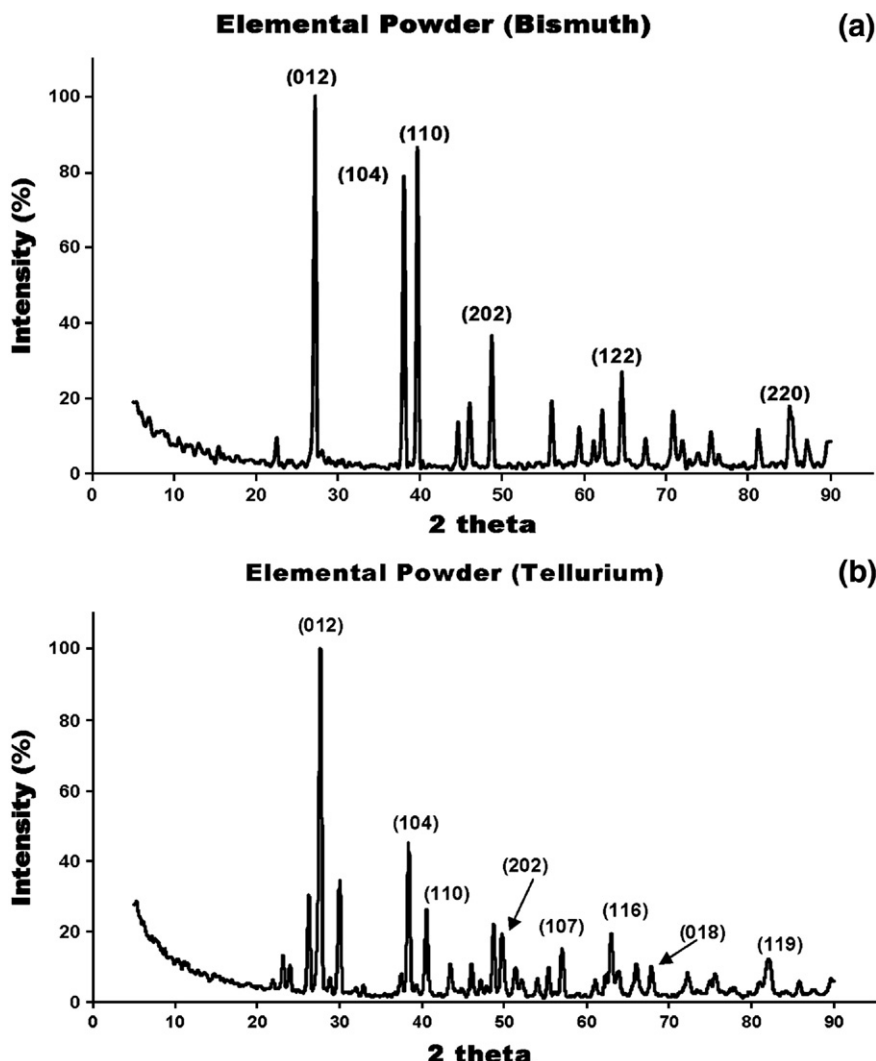


Fig. 3 – XRD spectra for the starting elemental powders. (a) bismuth, (b) tellurium, (c) antimony, (d) selenium.

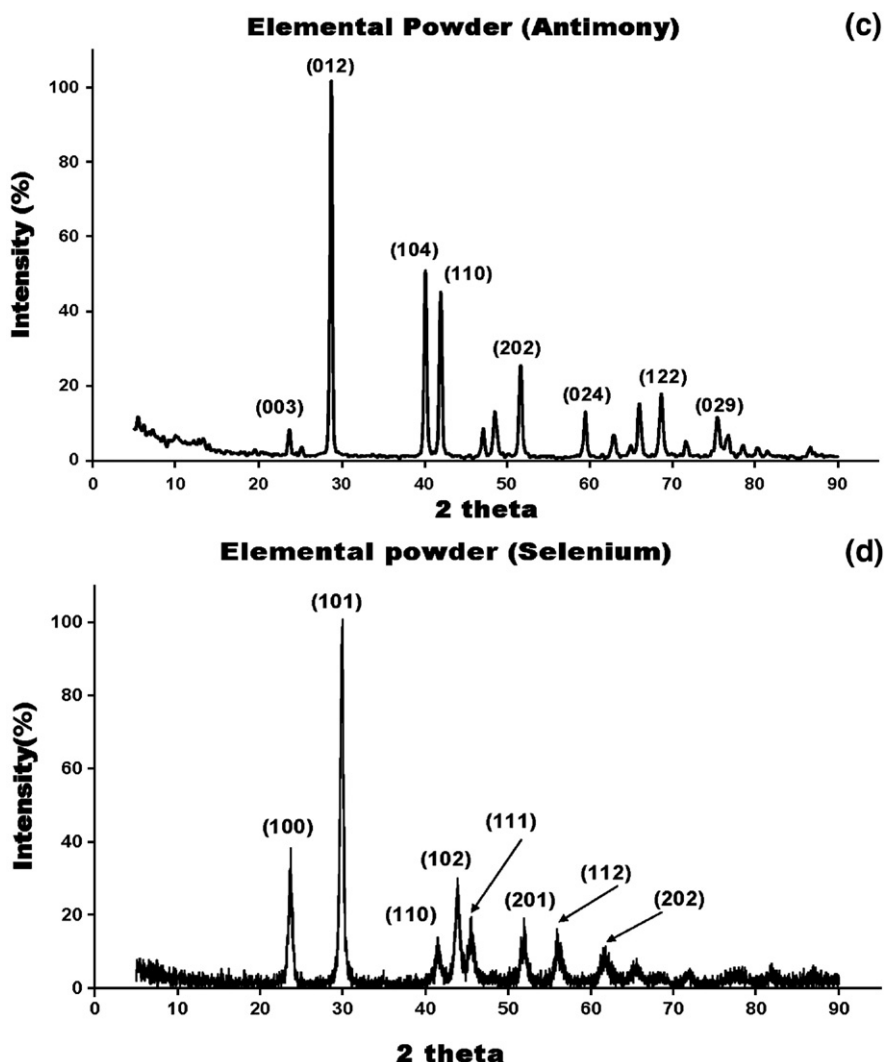


Fig. 3 (continued).

explosively consolidated monoliths, and conventional melt-grown samples using a Scintag XDS 2000 X-ray diffractometer and Cu K $\alpha$  X-radiation. The explosively consolidated monoliths and the conventionally (melt) grown solid samples were ground to correspondingly fine powder for XRD analysis. Afterward, these powders were compacted using petroleum jelly and placed on glass slides.

Shock-wave consolidated samples were prepared utilizing standard metallographic techniques and colloidal silica was used for final polishing; no etchant was required for these samples. Conventional, melt-grown samples were similarly prepared and etched using a solution consisting of 25 mL H<sub>2</sub>O, 7 mL HCl, and 3 mL H<sub>2</sub>O<sub>2</sub>. Samples were examined by light microscopy using optical metallurgy in a Reichert MEF4 AM optical microscope. The starting Bi and Te powders were also mounted in standard mounting material and ground and polished to reveal the powder interiors. The Vickers microindentation hardness of these powders was then measured using 10 and 25 gf loads, respectively (with 10 s dwell time), for a diamond indenter in a Shimadzu HMV-2000 digital microhardness tester. Measurements were also made using a 10 gf (0.1 N)

load on recognizable Bi and Te grains in the explosively consolidated materials in order to determine the hardness increment as a result of shock hardening. Similar measurements were also made for the melt-grown n- and p-type materials for comparison. Table 1 indicates the average starting microhardness values for the larger, Bi and Te particles.

The starting elemental powders in Table 1 were initially characterized in a Hitachi S-4800 field-emission scanning electron microscope (SEM). Phases or phase regions in the polished shock-wave and etched conventional melt-grown samples were analyzed in the SEM with an EDAX electron energy dispersive X-ray spectrometer. Surface analysis of the broken (fractured) shock-wave consolidated n- and p-type samples were also examined with the SEM.

Transmission electron microscopy (TEM) samples were prepared by fragmenting/crushing the shock-wave consolidated materials and conventional melt-grown n- and p-type semiconductors. The fragments were placed onto the surface of water in a Petri dish. The floating platelets or fragments (by surface tension effects) were gathered using a 3 mm, 200 mesh silicon monoxide/formvar-coated grid. A sandwich was

formed by laying a second coated grid on top of the supported specimens. The grids were placed on the standard holder and analyzed in a Hitachi H-8000 analytical TEM operated at 200 kV accelerating potential; utilizing a goniometer/tilt stage.

Thermoelectric properties (resistivity, Seebeck voltage, and thermal conductivity) were measured for the experimental samples using a 4-lead Kelvin method calibrated against known standards. Thermal conductivity ( $K$ ) was measured using a stainless steel reference series shunt compared to the experimental samples, eliminating the determination of actual heat flow through the samples: a thermal analog of the electrical Wheatstone bridge. Electrical conductivities were computed as reciprocals of the resistivity ( $\sigma=1/\rho$ ). The figure of merit ( $ZT$ ) was obtained by multiplying values of  $Z$  obtained by 300 K;  $Z=S^2\sigma/K$ .

### 3. Results and Discussion

Figs. 2 and 3 illustrate SEM views of the starting powder microstructures (size and size distribution: Table 1) and the corresponding XRD spectra, respectively. The XRD spectra (indexed from corresponding JCPDF data) illustrate prominent reflection planes marked, corresponding to crystal structures as

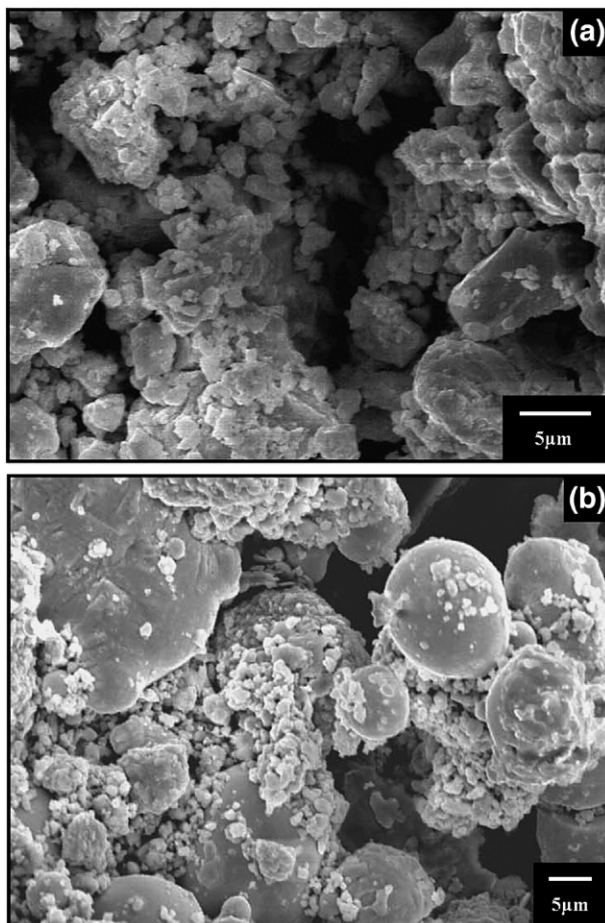


**Fig. 4 – SEM views of elemental powder mixtures (Table 1): (a) p-type mix (Te-Sb-Bi); (b) n-type mix (Bi-Te-Se).**

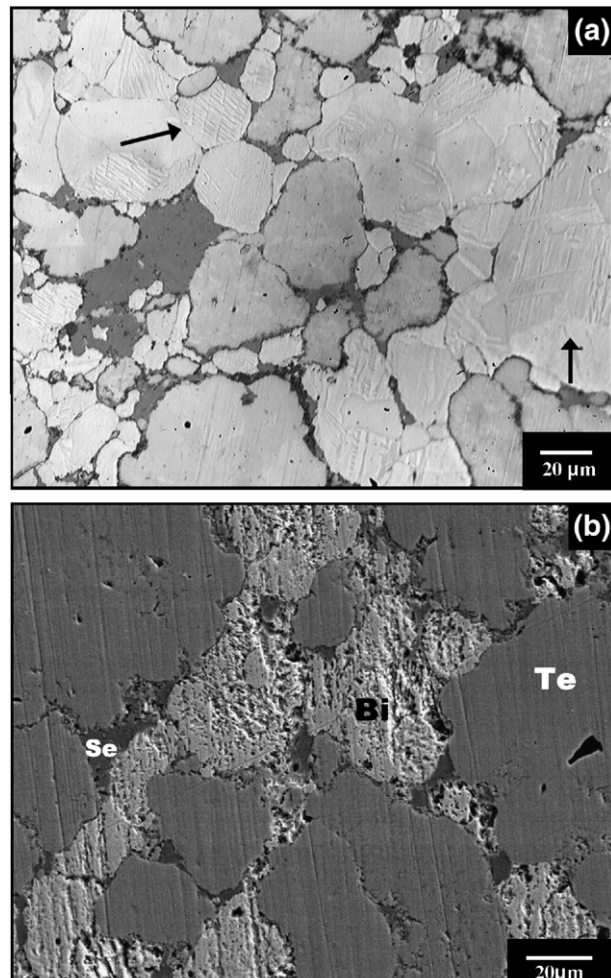


**Fig. 5 – n-type shock consolidated powder monolith. (a) optical microscopy image. (b) SEM image showing individual particle (grain) chemistries (from EDS).**

follows: Bi, rhombohedral (trigonal) —  $a=0.45$  nm,  $c=1.19$  nm; Te, rhombohedral (trigonal) —  $a=0.42$  nm,  $c=1.20$  nm; Sb, rhombohedral (trigonal) —  $a=0.43$  nm,  $c=1.13$  nm; Se, hexagonal —  $a=0.44$  nm,  $c=0.50$  nm. It should be noted that all of these elements are allotropic/polymorphic and the crystal structures are pressure-temperature sensitive. Fig. 4 shows SEM views for the mixed powders representing n-type and p-type, ternary-like systems (or mixtures) illustrated in Table 1, for comparison with Fig. 2. It is also noted that all but Se are highly anisotropic crystallographically. Rhombohedral  $\text{Bi}_2\text{Te}_3$  alloy ( $a=0.44$  nm;  $c=3.05$  nm; JCPDF 15-0863) is even more anisotropic.

Figs. 5 and 6 compare optical (light) microscopy views and SEM views of polished surface sections from the explosively consolidated powder mixtures represented in Fig. 4 for the n-type and p-type ternary-like systems, respectively. Figs. 7 and 8 show corresponding SEM and EDS analyses of areas which allowed specific grain or elemental areas to be identified as noted. In Figs. 7 and 8 the three-phase (elemental particle) mixtures are clearly delineated. The smaller fraction is Se and to some extent the small size regime of Bi for the corresponding n- and p-type mixtures, segregating along the

larger elemental particle fractions to create novel interfacial regimes as a consequence of the particle size distributions and mixture phenomena. It can also be noted in Figs. 5(a) (arrows) and 6(a–c) that shock-wave induced twinning occurs prominently in the Bi and Te particle grains, contributing additional interfacial scattering features for phonons [11]. These features are particularly notable in the magnified sequence in Fig. 6(a–c) where the inter-twin or interface spacing averages  $\sim 2 \mu\text{m}$ . Deformation twins in Figs. 5(a) and 6(a) are revealed by relief resulting by the mechanical polishing, which produces varying contrast. We did not observe or detect (by EDS) any evidence of shock-induced chemical reactions or alloying between individual (elemental) explosively consolidated powder particles (Figs. 5 and 6) [15, 16].

Fig. 9 compares a Vickers diamond microindentation in a Te starting particle cross-section (Fig. 9(a)) with a similar microindentation in a heavily twinned Te grain (Fig. 9(b)) in the p-type shock-consolidated monolith where the corresponding hardnesses were measured to be 0.46 GPa and 1.28 GPa for Fig. 9(a) and (b), respectively; or a microindentation hardness increase of  $\sim 178\%$  after shock consolidation for the Te. Note in Fig. 9(a) that the features shown are polishing scratches and not deformation twins as shown in Fig. 9(b).

Note also that the magnifications of Fig. 9(a) and (b) are essentially identical and the indentation size is characteristic of the microindentation hardness noted. Table 1 shows the average values of hardness measured for the larger, starting Bi and Te particles to be 0.18 and 0.56 GPa, respectively (Note that 1 VHN=0.01 GPa; where VHN is the Vickers hardness number measured from the diagonals of the pyramidal indentations shown in Fig. 9). Average measurements of the shock-induced Bi and Te hardness in the n-type consolidated monolith in Fig. 5 were 1.11 GPa and 1.21 GPa, respectively, while in the p-type consolidated monolith as in Figs. 6 and 9(b) the average values were 1.19 GPa and 1.43 GPa, respectively. Averaging the Bi grain measurements for both the n- and p-type shock consolidated monoliths resulted in a value of 1.15 GPa, or a hardness increase of 539% when compared with the average initial Bi particle hardness of 0.18 GPa, Table 1.

Twinning in Bi and Te has been described in earlier work by Cahn [17] and more recently in Bi crystals [18, 19], where twinning is favored because of the reluctance of Bi to deform by slip. Matsuo and Suzuki [19] noted that below about 20 K, dislocations ( $\sim 10^7/\text{cm}^2$ ) reduced the thermal conductivity of plastically deformed Bi crystals by 20% in contrast to

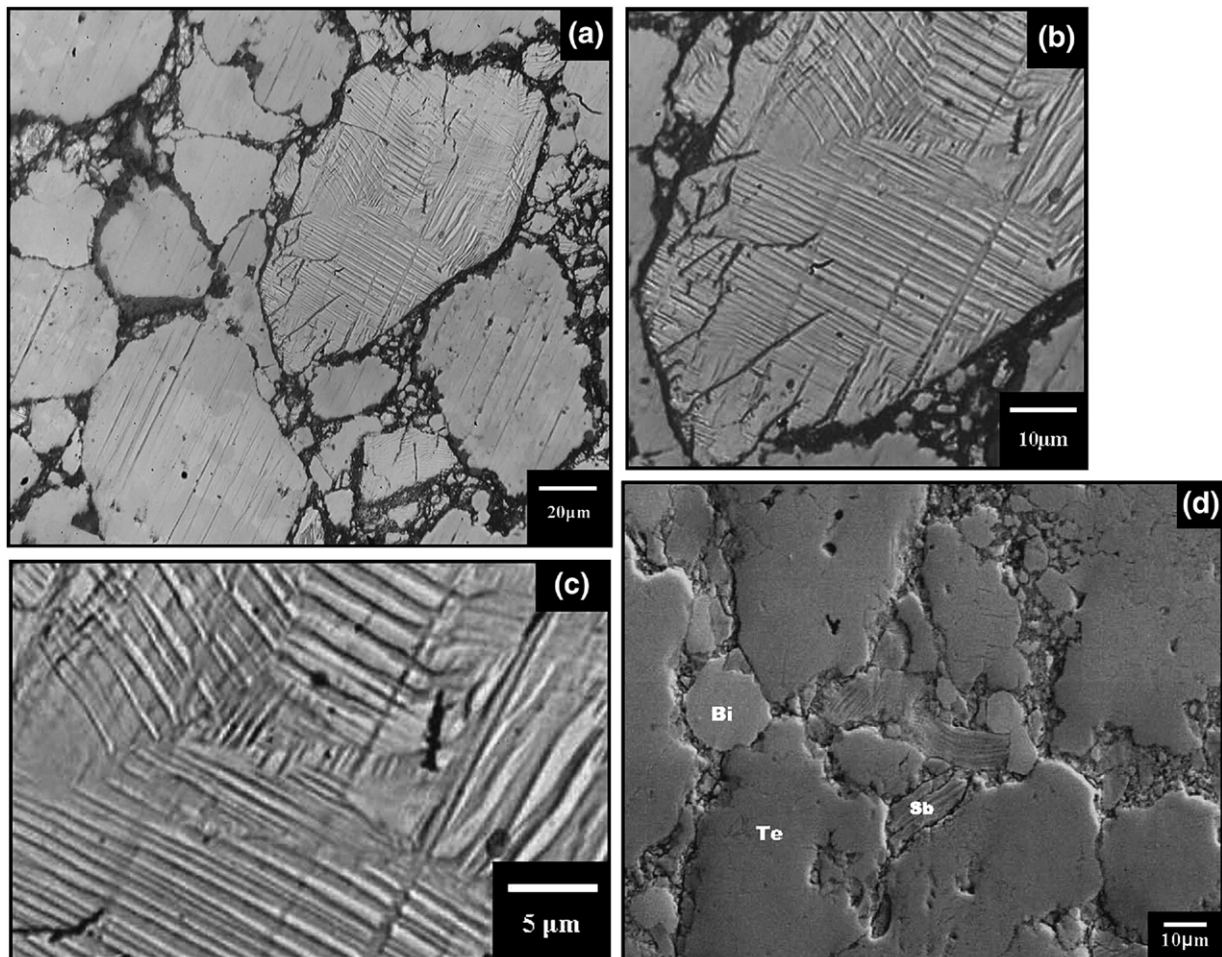


Fig. 6 – p-type shock consolidated powder monolith. (a) optical microscopy image. (b) and (c) show magnified views of deformation twins in (a). (d) SEM image showing individual particle (grain) chemistries (from EDS).

deformation twins or twin boundaries which decreased the conductivity by 30%. Earlier work involving plane shock of Bi polycrystalline samples in the pressure range of 2 to 5.5 GPa has also discussed the complexity of polymorphic transitions in light of the complex pressure-phase diagram (P-T diagram) characteristic of Bi [20, 21]. This pressure range is consistent with the consolidation pressure for this work as well. Polymorphic transitions in Te at high temperatures and pressures have also been discussed by Kennedy and Newton [22].

Fig. 10 compares fracture surface features for the explosively-consolidated mixtures along with corresponding EDS spectra identifying the elemental regions, while Fig. 11 shows comparative TEM bright-field images and superimposed selected-area electron diffraction (SAED) patterns for crushed fragments from the p-type, consolidated mixture (Fig. 10(c)). Dislocation structures are prominent in Fig. 11, where the dislocation density was estimated to be  $\sim 10^9/\text{cm}^2$  [23]. In Fig. 10(c) in particular the cleavage-like fracture shown prominently is associated with the shock-induced deformation twins illustrated in Fig. 6(c) and (d).

Figs. 12 and 13 compare the melt-grown, n- and p-type ternary systems, respectively, utilizing light microscopy and SEM imaging (including energy-dispersive X-ray spectrometry: EDS). Comparison of these microstructures with those produced by explosive consolidation in Figs. 5 and 6 provide a striking contrast for these thermoelectric materials systems. The melt-grown systems in Figs. 12 and 13 show very irregular grain structures and interface regimes (measuring  $<100\ \mu\text{m}$  to  $>500\ \mu\text{m}$ ) along with a wide range of stoichiometrically different structures, and eutectic phase regions prominently illustrated in the magnification sequence shown in Figs. 12(b and c) and 13(b and c). In Fig. 13(c) the likely eutectic is the Te-Sb (90–10% weight) [24]. The corresponding XRD spectra for these conventional melt-grown n-and p-type alloys are compared in Fig. 14, which provides an interesting contrast when compared to the XRD spectra for the shock consolidated powder mixtures shown in Fig. 15. It can be noted in Fig. 15 that some reflections overlap. For example, the Se (101) peak overlaps a corresponding Te peak at  $\sim 2\theta=30^\circ$  (compare Fig. 3(b) and (d)). In Fig. 14, prominent alloy peaks are indexed with the elemental XRD spectra shown in Fig. 3, but of course these alloy spectra are quite distinct from the elemental spectra. Both the n-and p-type melt-grown XRD spectra in Fig. 14 are characteristic of the trigonal (rhombohedral) crystal structure; the same as for Te, Bi, and Sb (Fig. 3a–c).

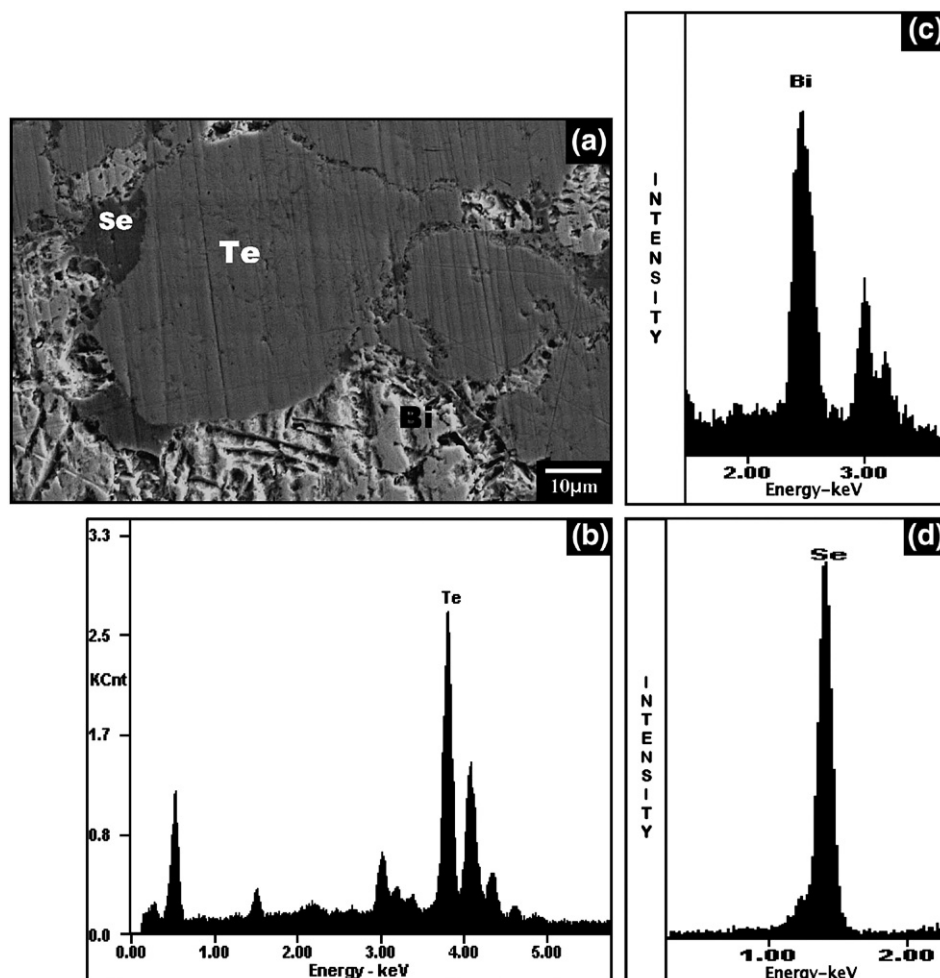
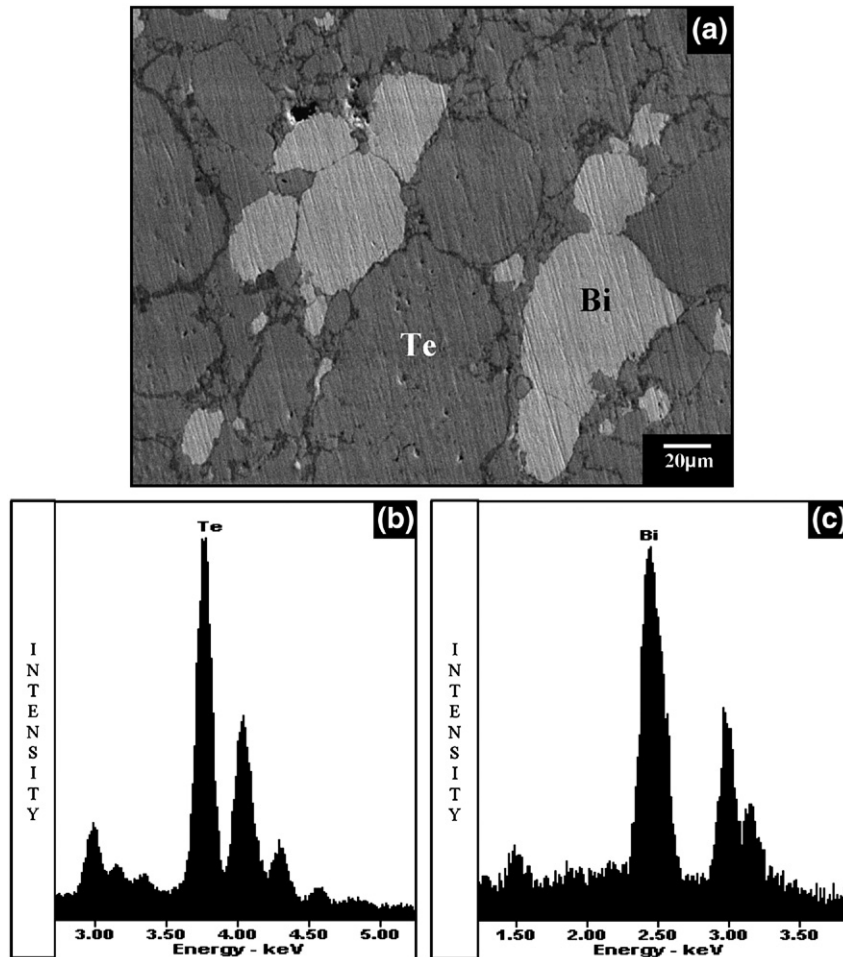


Fig. 7 – (a) SEM image and (b–d) corresponding EDS spectra illustrating the explosively consolidated n-type grain chemistries (Te, Bi, and Se), respectively, shown in (a).



**Fig. 8 – (a)** SEM image and (b and c) corresponding EDS spectra illustrating the explosively consolidated p-type grain chemistries (Te and Bi), respectively, shown in (a).

While Fig. 15 clearly illustrates the distinct 3-phase regions for the shock (explosively) consolidated n- and p-type powder mixtures in contrast to the ternary alloy n- and p-type melt-grown materials shown in Fig. 14, the melt-grown materials (Figs. 12 and 13) are themselves complex, multi-phase systems with eutectic phase interfaces serving to partition the grains in a manner similar to the shock-induced twin boundaries in the explosively consolidated powder mixtures (Figs. 5 and 6); providing scattering, especially for phonons [11]. Grain boundary influence on the electrical properties (resistivity in particular) of p-type Te has also been investigated recently by Berozovets et al. [25].

The similarity in the eutectic phase partitioning of grains in the melt-grown materials and the deformation twin partitioning in the Te and Bi, in particular in the explosively (shock) consolidated materials, is supported by corresponding Vickers microindentation hardness measurements where for the n-type, melt-grown material (Fig. 12) the average hardness measured in eutectic-containing grains was 0.85 GPa in contrast to “regular” grains where the average hardness was 0.60 GPa. Correspondingly, for the melt-grown, p-type material (Fig. 13), the average microindentation hardness measured in the eutectic-containing grains (Fig. 13(c)) was 0.93 GPa in contrast to

the “regular” grains where the average hardness was 0.42 GPa. This compares with an initial, average Bi particle microindentation hardness of 0.18 GPa (Table 1) in contrast to average Bi n-type shock consolidated grains of 1.11 GPa, and p-type shock consolidated grains of 1.19 GPa. This also compares with an initial, average Te particle microindentation hardness of 0.56 GPa (Table 1) in contrast to average Te n-type shock consolidated grains of 1.21 GPa and p-type shock consolidated grains of 1.43 GPa.

Fig. 16 shows, for comparison with Fig. 11, two TEM bright-field images and superimposed SAED patterns for a crushed fragment from the n-type, melt-grown material in Fig. 12. The dislocation structures were observed to be comparable to those shown for the explosively consolidated p-type, consolidated mixture in Fig. 11; dislocation densities ranged from  $10^9$  to  $10^{10} \text{ cm}^{-2}$ . Some areas of dislocation Moiré patterns are visible in Fig. 16(a) where the SAED pattern insert illustrates a nearly exact [111] orientation for BiTe (cubic;  $a=0.65 \text{ nm}$ ; JCPDF 15-0820); characteristic of the wide range of stoichiometries illustrated previously in Figs. 12 and 13. It might be noted that heterogeneous dislocation distributions ranging from  $10^6$ – $10^{10} \text{ cm}^{-2}$  were earlier observed in polycrystalline, melt-grown Te subjected to compression [26].

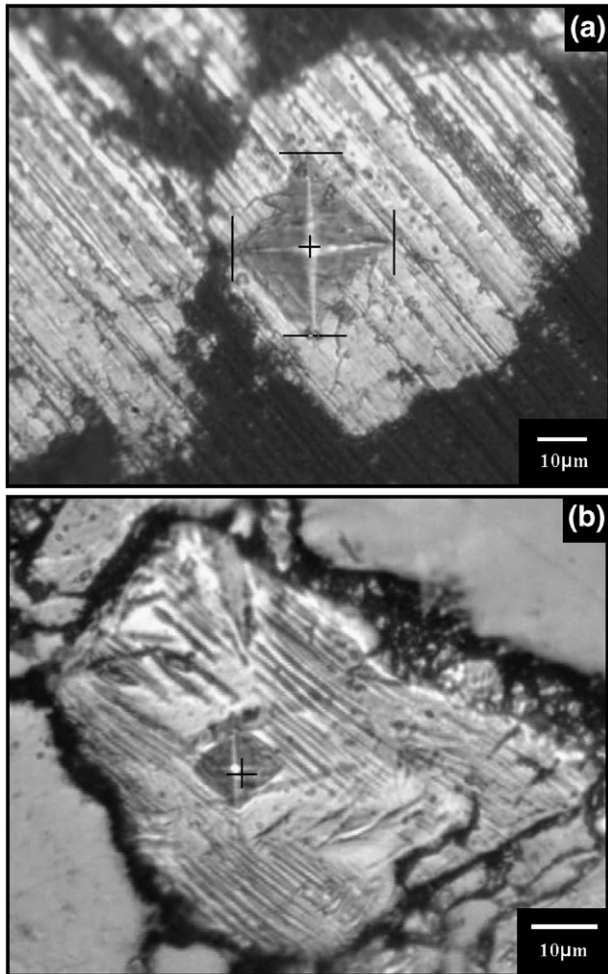


**Fig. 9 – Light microscopy images of Vickers diamond indentation (a) in a Te particle and (b) in a Te grain in the p-type shock consolidated monolith. The indentation in (a) corresponds to a Vickers hardness of 0.46 GPa while in (b) it corresponds to 1.28 GPa. (10 gf (0.1 N) load; 10a).**

While we were successful in creating novel shock-consolidated 3-phase monoliths and comparing them microstructurally with conventional, melt-grown, n- and p-type thermoelectric alloys based on doped Bi–Te ( $\text{Bi}_2\text{Te}_3$ ), the measurements of key thermoelectric properties, namely S and ZT in particular, were not encouraging for the shock-consolidated n- and p-type monoliths as illustrated in the results in Table 2. Although shock consolidation creates a plethora of interfacial scatterers (e.g. Figs. 5, 6, 9(b)) it does not create the excess or deficiency of electrons required (as a consequence of elemental (atomic) substitutions) to define an efficient thermoelectric device; especially since both  $\sigma$  and S decrease, and  $S^2$  is especially reduced. However the noticeable decrease in the thermal conductivity for the shock consolidated materials in Table 2 is encouraging, although not understood.

In Table 2 we have also compared the average shock-consolidated n-type and p-type microindentation hardnesses (by averaging the Bi and Te averages, respectively, noted earlier) along with the melt-grown n-type and p-type micro-indentation hardness averages for all grains (regular and

eutectic-containing). While the shocked materials are considerably harder, reflecting significantly more defects (presumably deformation twin interfacial microstructures), the thermoelectric property measurements, although indicating some thermoelectric response, are not significant, indicating a detrimental effect of the shock-induced defects. This may also be true for the eutectic phases in the melt-grown material especially since the n-type melt-grown material exhibited a ZT roughly only 20% of the current, achievable value of ~1 [27].

#### 4. Summary and Conclusions

The microstructures and thermoelectric properties of explosively (shock-wave) consolidated 3-phase monoliths of powder mixtures corresponding to n-type and p-type stoichiometries ( $\text{Bi}_{2.7}\text{Te}_{0.3}$  and  $\text{Bi}_{0.5}\text{Te}_{3}\text{Sb}_{1.5}$ , respectively, based on the  $\text{Bi}_2\text{Te}_3$  system) have been compared with identical stoichiometric melt-grown semiconductor alloys. The shocked materials exhibited significantly lower Seebeck voltages and thermoelectric figures of merit (ZT) than the conventional melt-grown alloys, although the melt-grown alloys exhibited thermoelectric figures of merit less than half contemporary values [27]. The shock-consolidated monoliths exhibited considerable deformation twinning, particularly in the large Bi and Te grains. Comparative Vickers microindentation hardness measurements reflected these shock-induced microstructures: the initial Bi and Te powder particle hardnesses averaged 0.18 GPa and 0.56 GPa, respectively, in contrast to average hardness values for the n-type and p-type shock consolidated materials of 1.15 GPa and 1.31 GPa, respectively. These microindentation hardness values were essentially twice the values for the corresponding n- and p-type, melt-grown materials which were 0.72 GPa and 0.68 GPa, respectively.

TEM measurements of dislocation densities in both the shock-consolidated and melt-grown materials indicated values ranging from  $\sim 10^9$  to  $10^{10} \text{ cm}^{-2}$ . The melt-grown n- and p-type thermoelectric materials exhibited a wide range of stoichiometries from grain-to-grain, and included many grains containing eutectic phases which produced a grain refinement similar to that produced by deformation twins in individual grains of the shock-consolidated materials. It is believed that it is the eutectic interfaces along with the grain boundaries, which, like deformation twins and phase boundaries in the shocked materials, decrease the electrical conductivity while simultaneously decreasing the thermal conductivity. What we had hoped was that these interfacial defects would alternatively increase electrical conductivity by increasing the mean free path while decreasing thermal conductivity. The decrease in the Seebeck coefficient was also unexpected.

These results point up the fact that homogeneous semiconductor systems are probably not achieved in melt-grown thermodynamic materials based on appropriately doped  $\text{Bi}_2\text{Te}_3$ . Novel mixture fabrications such as shock-consolidation, involving the production of a high density of interfaces, including sub-micron grain sizes, were also found to be inadequate. Rapid prototyping/controlled layer rapid manufacturing, ultrasonic and microwave consolidation or

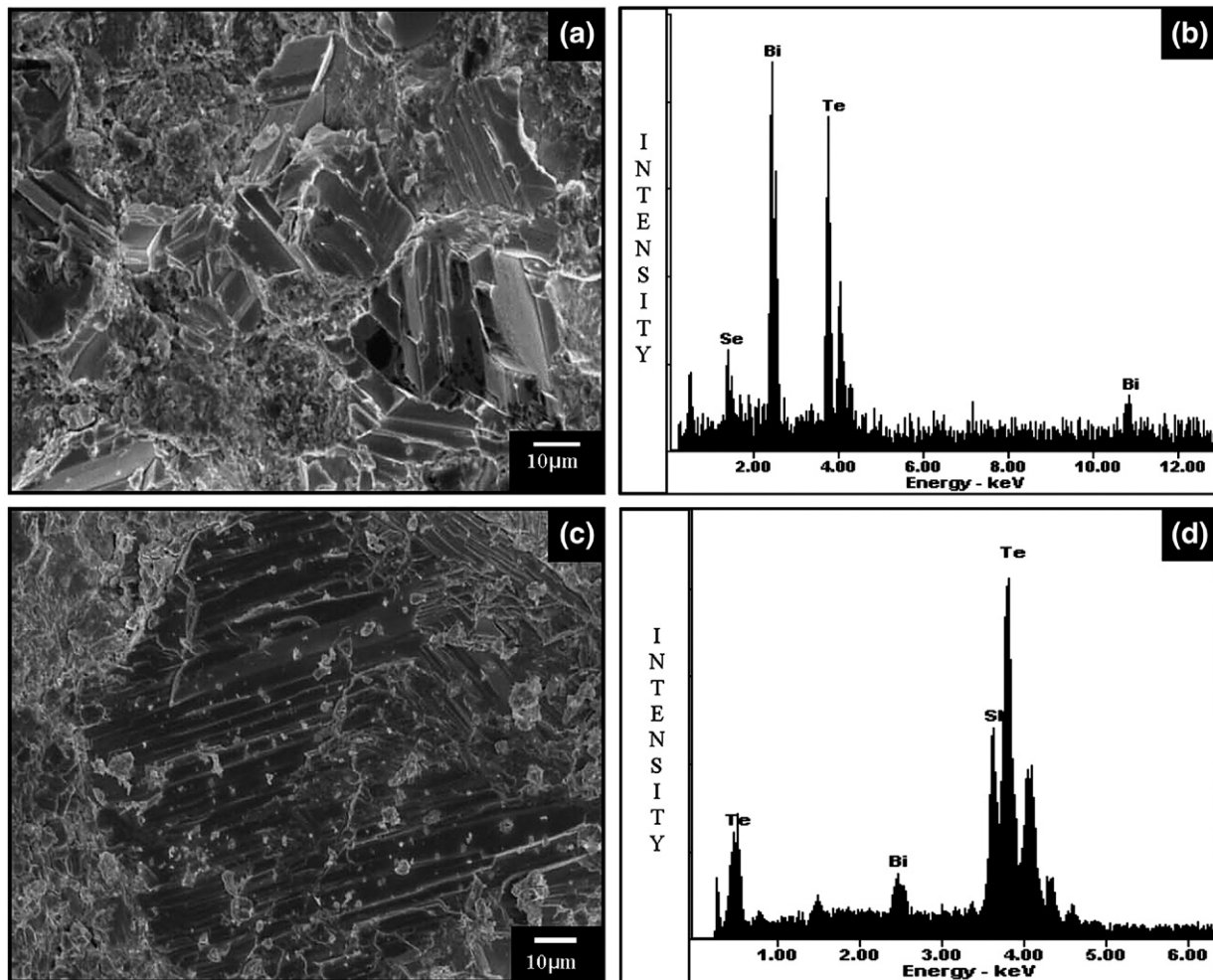


**Fig. 10 – (a)** Fractograph and **(b)** XRD spectrum of the n-type explosively consolidated monolith after crushing. **(c)** Fractograph and **(d)** XRD spectrum of the p-type explosively consolidated monolith after crushing.

sol-gel/aerogel technologies may offer more efficient fabrication alternatives if inefficient scattering of electrons and phonons can be avoided.

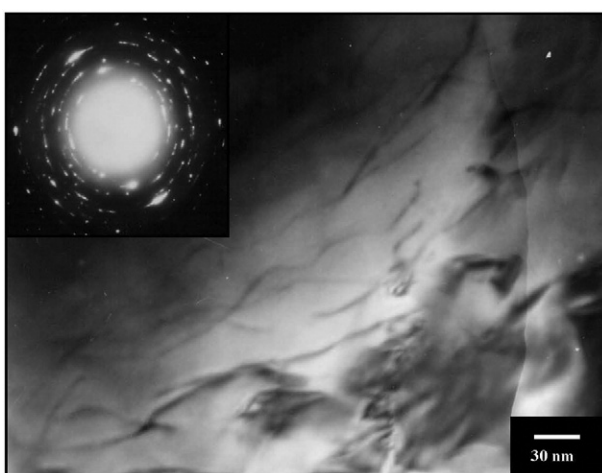


**Fig. 11 –** TEM bright-field image and superimposed selected-area electron diffraction (SAED) pattern for crushed fragments from the p-type, consolidated mixture (Fig. 10(c)).

## Acknowledgment

This research was supported by a Mr. and Mrs. MacIntosh Murchison endowment at The University of Texas at El Paso. We are grateful for the help of David Brown in fabricating the explosive consolidation tooling.

## R E F E R E N C E S

- [1] Rowe DM, editor. CRC handbook of thermoelectrics. Baton Rouge: CRC; 1995.
- [2] Holas GS, Sharp J, Goldsmid HJ. Thermoelectrics: Basic Principles and New Materials Development. Heidelberg: Springer-Verlag; 2001.
- [3] Majumdar A. Thermoelectricity in semiconductor nanostructures. *Science* 2004;303:777–82.
- [4] Li DY, Wu Y, Fan R, Yang P, Majumdar A. Thermal conductivity of Si/SiGe superlattice nanowires. *Appl Phys Lett* 2003;83:3186–91.
- [5] Kim W, Zide J, Gossard A, Klenov D, Stemmer S, Shakouri A, Majumdar A. Thermal conductivity reduction and thermoelectric figure of merit increase by embedding nanoparticles in crystalline semiconductors. *Phys Rev Lett* 2006;96:045901-1-4.

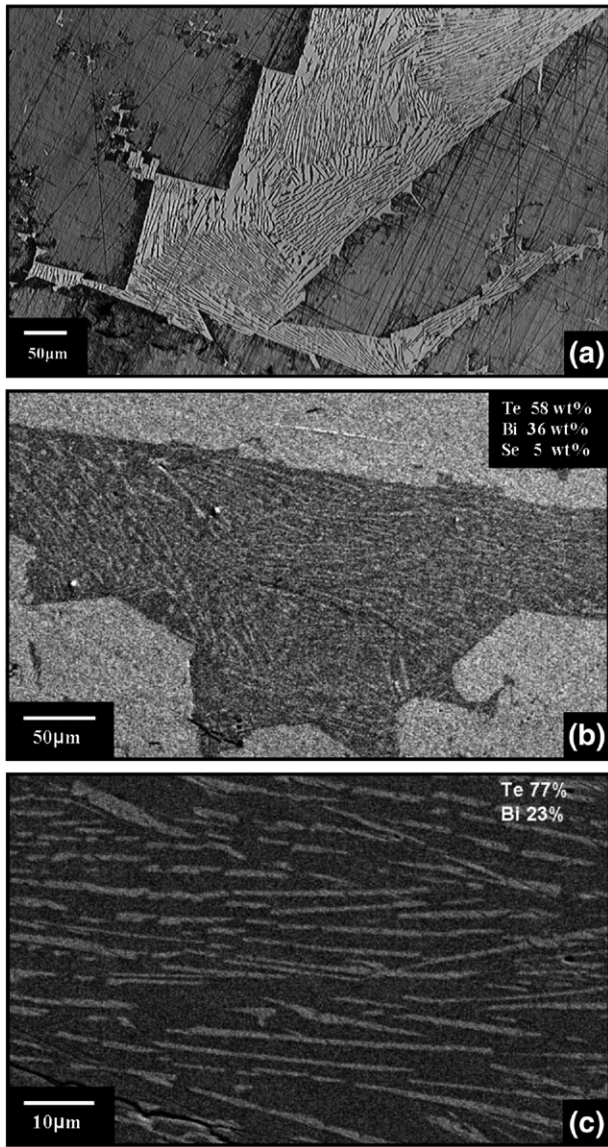


**Fig. 12 – n-type melt-grown thermoelectric alloy.** (a) Optical microscopy image. (b) SEM image. (c) Magnified SEM view in the eutectic region in (b). The overall weight percent elemental compositions shown in (c) are from EDS analysis.

- [6] Kim W, Wang R, Majumdar A. Nanostructuring expands thermal limits. *Nanotoday* 2006;2(1):40–7.
- [7] Costescu RM, Cahill DG, Fabreguette FH, Sechrist ZA, George SM. Low thermal conductivity in W/Al<sub>2</sub>O<sub>3</sub> nanolaminates. *Science* 2004;303:989.
- [8] Zou J, Kotchetkov D, Blandin AA. Thermal conductivity of GaN films: effects of impurities and dislocations. *J Appl Phys* 2002;92:2534–41.
- [9] Savvides N, Goldsmid HJ. The effect of boundary scattering in the high-temperature thermal conductivity of silicon. *J Phys* 1973;C6:1701–6.
- [10] Slack GA, Hussain MA. The maximum possible conversion efficiency of silicon–germanium thermoelectric generators. *J Appl Phys* 1991;70:2694–9.
- [11] Kanatzidis MG, Mahanti SD, Hogan TP, editors. *Chemistry, physics, and materials science of thermoelectric materials: beyond bismuth telluride*. New York: Kluwer Academic/Plenum Publishers; 2002.

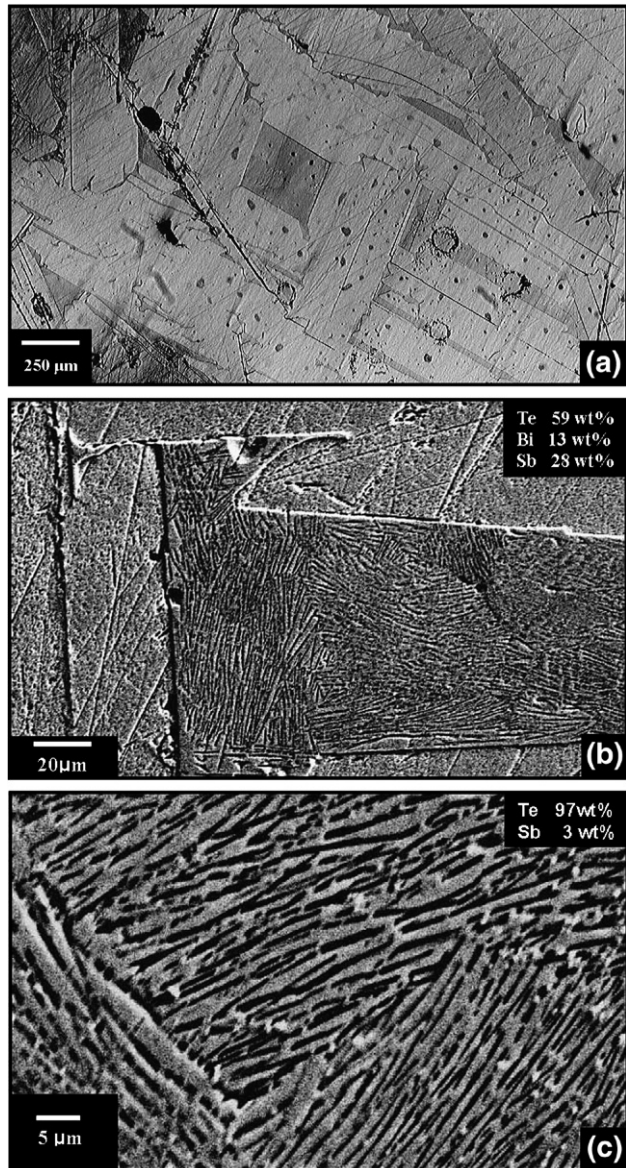


**Fig. 13 – p-type melt-grown thermoelectric alloy.** (a) Optical microscopy image. (b) SEM image. (c) Magnified SEM view of the eutectic region in (b). The overall weight percent elemental compositions shown in (c) are from EDS analysis.

- [12] Prümmer R. *Explosivverdichten Pulvriger Substanzen*. Berlin: Springer-Verlag; 1987.
- [13] Meyers MA, Wang SL. An improved method for shock consolidation of powders. *Acta Metall* 1988;36:925–36.
- [14] Murr LE, editor. *Shock waves for industrial applications*. Park Ridge, NJ: Noyes Publications; 1988.
- [15] Murr LE, Staudhammer KP. Shock wave sensitization, shock-induced reactivity, and new materials fabrication, Chap. 12, *ibid*, p. 441.
- [16] Thadhani NN. Shock-induced and shock-assisted solid-state chemical reactions. *J Appl Phys* 1994;76:2129–35.
- [17] Cahn RW. Twinned crystals. *Adv Phys* 1954;3(12):363.
- [18] Ostrikov OM. Magnetoplastic effect upon twinning of bismuth single crystal. *J Appl Tech Phys* 2001;42(3):515–21.
- [19] Matsuo T, Suzuki H. Effect of plastic deformation on the thermal conductivity of bismuth crystals. *J Phys Soc Japan* 1976;41:1692–6.

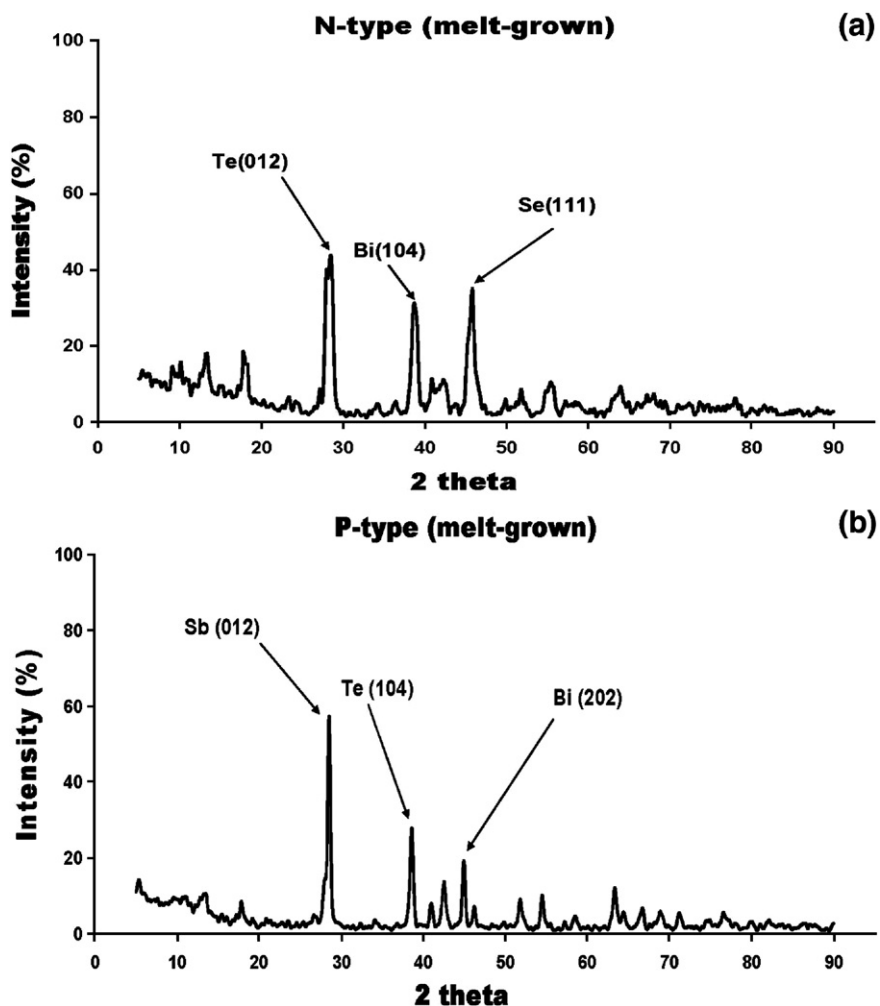


**Fig. 14–** XRD spectra corresponding to the melt-grown (a) n-type and (b) p-type thermoelectric materials. Prominent peaks are indexed for the principal ternary elements (Table 1) for these structures.

- [20] Rosenberg Z. Determination of the dynamic phase transitions in bismuth with in-material manganin gauges. *J Appl Phys* 1984;56:3328–33.
- [21] Dormevel R, Perroud J, Remist C. Phase transition and Hugoniot data in shock loaded bismuth. In: Meyers MA, Murr LE, Staudhammer KP, editors. Chap. 93 in Shock-wave and high-strain-rate phenomena in materials. New York: Marcel Dekker, Inc.; 1992. p. 997.
- [22] Kennedy GC, Newton RC. Solid–liquid and solid–solid phase transitions in some pure metals at high temperatures and pressures. In: Paul W, editor. Chap. 7 in Solids under pressure. New York: McGraw-Hill Book Co., Inc.; 1963. p. 163.
- [23] Murr LE. Electron and ion microscopy and microanalysis: principles and applications. 2nd Edition. NY: Marcel Dekker, Inc.; 1991.
- [24] Staudhammer KP, Murr LE. Atlas of binary alloys. New York: Marcel Dekker, Inc.; 1973.
- [25] Benezovets VA, Farbshtain II, Parfenies RV, Yakimov SV, Nizhankouskii VI. Grain boundary influence on the electrical properties of tellurium microstructures ingots and nanocluster crystals. *Mat Sci Forum* 2006;508:25–37.
- [26] Broniatowski A, Faivre G. Study of dislocations in deformed Te by electron microscopy. *Philos Mag* 1974;30:765–71.
- [27] Yamashita O, Tomiyoshi S. High performance N-type bismuth telluride with highly stable thermoelectric figure of merit. *J Appl Phys* 2004;95(11):6277–84.

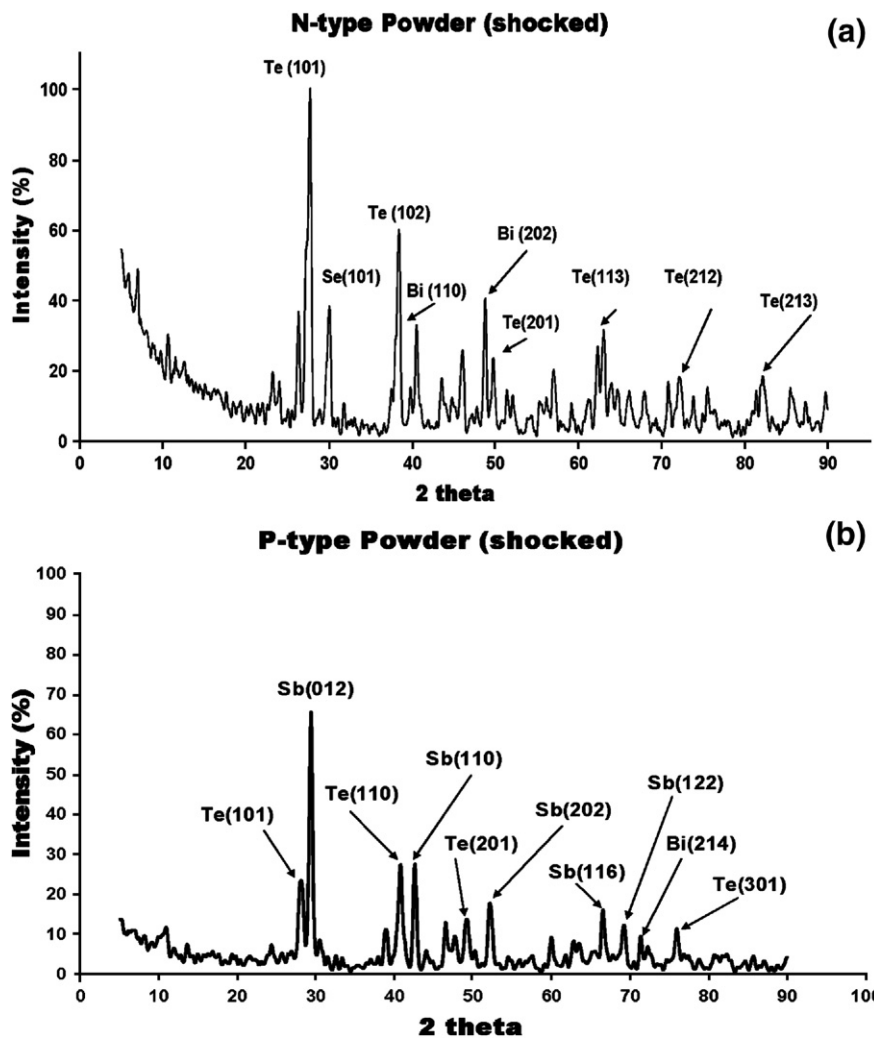
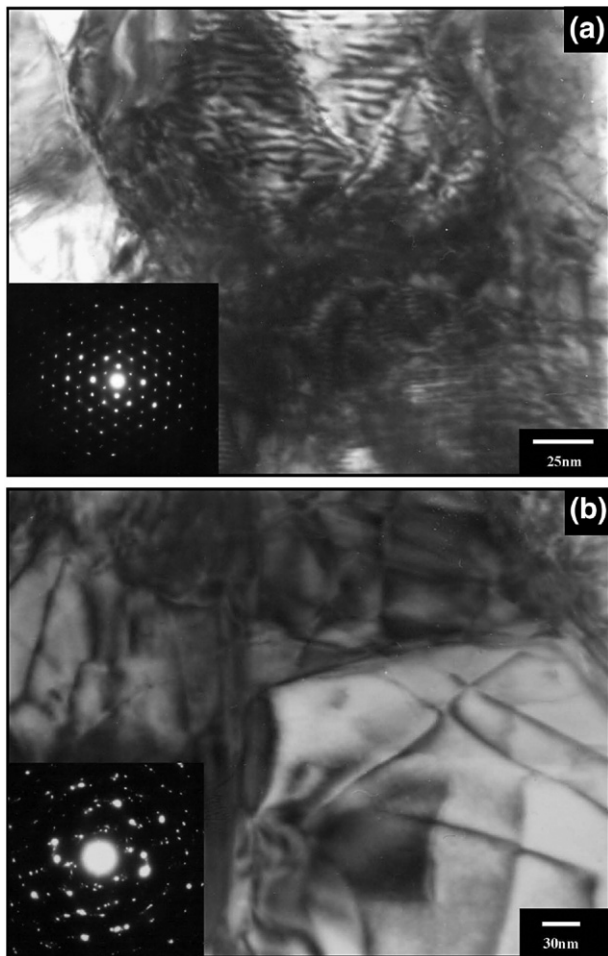


Fig. 15 – XRD spectra corresponding to the explosively (shock) consolidated (a) n-type and (b) p-type thermoelectric monoliths. Prominent peaks are indexed for the principal ternary elements (Table 1) for these structures.



**Fig. 16 – (a and b)** TEM images and SAED patterns for a crushed fragment from the n-type, melt-grown material.

**Table 2 – Property measurements**

Material type	$S$ ( $\mu\text{V/K}$ )	$\sigma$ ( $\Omega\text{cm}^{-1}$ )	$K$ ( $\text{W/cm K}$ ) <sup>a</sup>	$ZT$ (300 K)	Hardness (GPa)
Shocked n-type	-79	125	0.028	0.0086	1.15 <sup>b</sup>
Shocked p-type	16	40	0.024	0.0001	1.31 <sup>b</sup>
Melt-grown n-type	-160	583	0.053	0.0849	0.72 <sup>c</sup>
Melt-grown p-type	174	827	0.036	0.2076	0.68 <sup>c</sup>

<sup>a</sup>  $K = (K_{e1+} K_{ph})$ .

<sup>b</sup> Average of Bi and Te grains in the shock consolidated samples. 8 indentations for each elemental grain type; with two diagonal measurements for each indentation (Fig. 9).

<sup>c</sup> Average of all grains, including those exhibiting eutectic microstructures in the melt-grown samples. 8 indentations in regular grains; 8 indentations in eutectic grains; with two diagonal measurements for each indentation.